New routes for improving adhesion at the metal/α-Al2O3(0001) interface

Rémi Cavallotti, Ha-Linh Thi Le, Jacek Goniakowski, Rémi Lazzari, Jacques Jupille, Alexey Koltsov, Didier Loison

New routes for improving adhesion at metal/α-Al_2O_3(0001) interface.†

Rémi Cavallotti,[abc] Ha-Linh Thi Le,[ab] Jacek Goniakowski,*[ab] Rémi Lazzari,[ab] Jacques Jupille,[ab] Alexey Koltsov,[c] and Didier Loison[c]

With the advent of new steel grades, the galvanic protection by zinc coating faces a new paradigm. Indeed, enrichment in strengthening elements prone to oxidation such as Al, Mn, and Si, leads to the formation of oxide films that are poorly wet by zinc. We study herein routes for improvement of adhesion at the model Zn/α-Al_2O_3 interface by metallic additions. As a first step, with help of *ab initio* results on adsorption characteristics of transition metal adatoms at α-alumina surfaces, we establish and rationalize clear trends in the behavior of both metal-alumina interaction strength and in the relative thermodynamic stability of configurations with weakly and strongly bound metal adatoms. The reasons of enhanced binding strength of transition metals, such as Cr, maintained regardless the precise alumina termination and surface charge state are pointed out. On these grounds, possible improvements of adhesion in realistic conditions are discussed. It is predicted that an enrichment in transition metals, such as Cr, may produce strongly adhesive interfaces that lead to cohesive cleavage.

1 Introduction

The hindrance of a widespread use of many materials by a low corrosion resistance is a strong concern for the physical chemistry of surfaces and interfaces. In response, an important research effort has been devoted to conceptualize inorganic and organic coatings,[1–3] sol-gel films,[4] and surface treatments,[5] with a strong focus on pure and alloyed metals that are prone to oxidation. One such a case is the galvanic protection of iron-based materials by zinc which has long-proved its efficiency since zinc, being less noble or anodic than iron, sacrificially corrodes to protect the substrate steel.[6] In practice, steel strips are coated with a zinc layer by either zinc electro-deposition on annealed steel sheets or by hot-dip galvanization, which combines annealing and coating into a single process.[6,7] Indeed, before applying the protective zinc coating, cold-rolled steel strips undergo a recrystallisation annealing, at about 800°C in a reducing N_2-5%H_2 atmosphere to reduce stress and residual iron oxides.[6,8–10]. However, more recently, new steel grades, known as advanced high strength steels (AHSS), are purposely enriched in strengthening elements, such as Al, Si and Mn,[11–15] so that manufacturing thinner steel sheets allows the reduction of cost and, above all, of weight, as to meet the environmental imperative of reduction of CO_2 emission in automotive industry. Indeed, recrystallization of AHSS strips at 800°C results in the selective oxidation of the electropositive alloyed elements. The poor wetting by zinc alloys of the oxide particles or films segregated at the steel surface reduces dramatically the quality of the anti-corrosive Zn protection.[6,10] Typically, a 1.5-8 wt. % enrichment of steel with aluminum, may lead to a formation of a quasi-continuous alumina film at the surface, which efficiently impedes zinc adhesion in the standard hot-dip galvanization process. While practical possibilities of a complete removal of such surface oxides are being investigated, search of routes for an efficient improvement of adhesion at zinc/alumina interfaces has become one of key issues of steel surface protection. Indeed, the galvanization faces a new paradigm, since it switches from what is close to a reactive interface with a bare iron surface[6,7] to a high-energy interface with wide band-gap oxides.

The case examined herein is that α-Al_2O_3(0001) surface which is a reference for the study of metal-oxide interfaces[16–24]. Alumina is also among the oxides which commonly appear in selective oxidation.[6] Despite such strong applicative interest and the widespread use of sapphire in the growth of epitaxial zinc oxide layers,[25] the interaction of zinc with alumina has received only little attention in the past.[26,27] In our recent theoretical study,[28] we have considered the adsorption of isolated Zn adatoms on different bare and hydroxylated terminations of the α-Al_2O_3(0001) surface, with surface characteristics similar to the more complex γ-alumina crystallites, which has been identified in model steel oxidation experiments.[29] We have shown that, in non-extreme oxygen-rich conditions, Zn may preferentially spill over the alumina substrate as an array of strongly adsorbed adatoms, rather

[a] *CNRS, UMR 7588, Institut des Nanosciences de Paris, F-75005 Paris, France. Fax: ; +33 (0)1 44 27 39 82 Tel: +33 (0)1 44 27 46 17; E-mail: Jacek.Goniakowski@insp.jussieu.fr*

[b] *Sorbonne Universités, UPMC Univ Paris 06, UMR 7588, INSP, F-75005 Paris, France.*

[c] *ArcelorMittal Maizières Research, voie Romaine, F-57280, Maizières lès Metz, France.*

† Electronic Supplementary Information (ESI) available: structural data of key configurations. See DOI: 10.1039/b000000x/

than aggregate in metallic clusters weakly bound to the substrate. However, such strong bonding was predicted to occur only at either the polar oxygen-rich alumina termination, or the stoichiometric termination with a net surface charge induced by an excess of surface hydroxyls.[28]

In the present work, we systematically scrutinize the interaction of alumina with metal adatoms from across the first transition series (Cr, Co, and Ni) and with the late transition and noble metals such as Cu and Ag. With a strong concern to model systems that can be encountered in realistic conditions, we focus in a comprehensive manner on the most representative surface configurations of adatoms on bare and hydroxylated alumina surfaces. On this grounds we establish and rationalize a clear trend in the behavior of both metal-alumina interaction strength (Section 3) and in the relative thermodynamic stability of weakly and strongly bound configurations (Section 4). We point out an enhancement of the binding strength for transition metals, such as Cr, which is maintained regardless the precise polar character of surface termination and/or its hydroxylation state. A discussion of routes for improvement of adhesion of Zn on alumina is given (Section 5), including an analysis of interface resistance at extended Zn/alumina interfaces with and without an interfacial Cr buffer. We predict that enrichment in Cr may produce strongly adhesive interfaces, similar to those obtained by metal deposition at polar alumina termination.

2 Computational method and settings

All computational results were obtained within Density Functional Theory (DFT), implemented in VASP (Vienna ab initio simulation package),[30,31] with projector augmented wave (PAW) method[32,33] to describe the interaction of valence electrons with atomic cores. Several different types of approximation to the exchange-correlation functional were used as to validate the calculated trends in metal-oxide interaction strength: local density approximation (LDA-CA)[34], generalized gradient approximation (GGA-PW91),[35] dispersion-corrected GGA (optB88-vdW),[36–38] and GGA+U.[39]

Two terminations of the basal Al_2O_3(0001) surface, with different polarity characteristics have been considered:[28,40,41] the non-polar stoichiometric surface terminated by a single Al plane (stacking sequence Al/3O/Al-Al/3O/Al-etc. per (1×1) surface unit cell) and the polar oxygen-rich surface terminated by the O plane (stacking sequence 3O/Al-Al/3O/Al-etc.), Fig. 1. In the following we refer to these two terminations as (Al) and (3O), respectively. In all calculations, a 8x8x1 Monkhorst Pack grid was used for k-point sampling of the Brillouin zone of the (1×1) surface unit cell. All structures were fully relaxed until residual forces dropped below 0.01 eV/Å. Ionic charges were estimated with the partition scheme proposed by Bader.[42–44]

Isolated metal adatoms. Adsorption of isolated metal adatoms was modeled with alumina slabs composed of six -Al/3O/Al- units, with adspecies adsorbed symmetrically at both slab surfaces. To avoid spurious interactions between periodic images, the slabs were separated by at least 10 Å of vacuum. In the case of the bare (Al) termination, the (1×1) surface unit cell has been systematically used, providing a 4.7 Å distance between periodic

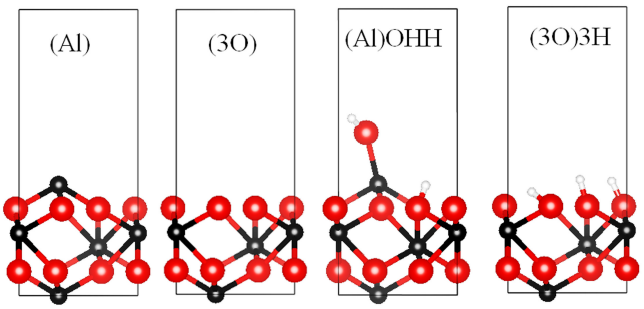

Fig. 1 Schematic representation of the (1×1) surface unit cells of Al_2O_3(0001) terminations considered in the present study: bare stoichiometric (Al) and oxygen-rich (3O) terminations; fully hydroxylated stoichiometric (Al)OHH and fully hydrogenated oxygen-rich (3O)3H terminations. Oxygen, aluminum, and hydrogen atoms are represented with red, black, and white circles, respectively.

adsorbate images, much larger than the interatomic distances in the corresponding metal bulk crystals. Conversely, since metal adsorption on the (3O) surface results in ionization of adatoms and in a formation of surface M^{+n} species,[28] adsorption in the (1×1), (1×2), and (2×2) surface unit cells has been considered as to identify configurations of the lowest formation energy (see Section 4). The resulting *optimal* series of configurations, includes Cr in the formal +3 oxidation state [obtained with a single adatom per (1×1) cell] and Co, Ni, Cu, Ag, and Zn in the formal +2 oxidation state [obtained with three metal adatoms per (1×2) cell].

In the case of hydroxylated (Al) and (3O) terminations, Fig. 1, the oxidation state of the adatoms depends additionally on the density of surface OH^- groups.[28] The calculated lowest energy (optimal) series includes Co, Ni, Cu, Ag, and Zn in the formal +2 oxidation state [obtained with (Al)$OHM_{0.5}$ and (3O)HM per (1×1) cell, respectively] and Ag in the formal +1 oxidation state [obtained with (Al)OHM and (3O)2HM per (1×1) cell, respectively]. Cr favors formal +2 oxidation state at the hydroxylated (Al) termination [(Al)$OHM_{0.5}$ per (1×1) cell] and +4 state at the hydroxylated (3O) surface [(3O)HM per (1×1) cell, achieved due to a negative charging of surface H, which binds directly to the metal adatom].

Metal/alumina interfaces. Simulations of metal/alumina interfaces, intended to provide a preliminary information on the interface resistance (Section 5), were performed on a periodic superstructure composed of six -Al/3O/Al- units sandwiched with nine atomic layers of Zn, with two equivalent interfaces per unit cell. Due to its relatively small size and a moderate (<3%) mismatch between the two lattices, all interface calculations employed a (1×1)-Al_2O_3(0001) // $(\sqrt{3}\times\sqrt{3})$ $R30^\circ$-Zn(0001) coincidence cell. The in-plane lattice parameters were fixed to those calculated for bulk alumina. Moreover, as to highlight the role of Cr on the interface adhesion, we have considered buffer layers of one, two or three (111) planes of Cr at the interface. Within the supercell used in calculations it requires a ∼10% expansion of the in-plane Cr-Cr distances with respect to those in the bulk metal. This spurious effect is to a large extent compensated by a spontaneous contraction of the inter-plane Cr-Cr distances. Distances between subsequent atomic planes and the interface dis-

tances were optimized by relaxing the supercell lattice parameter in the direction perpendicular to the interface. The interface registries between the materials and the positions of all atoms in the unit cell were also optimized.

3 Binding of metal adatoms to alumina surfaces

Figures 2 and 3 summarize the calculated adsorption characteristics of metal M adatoms on the bare (3O) and (Al) terminations of alumina. Adsorption energies per adsorbate $E_{\rm ads} = -(E_{\rm slab+nM} - E_{\rm slab} - nE_{\rm M})/n$ were deduced from total energies of alumina slabs with ($E_{\rm slab+nM}$) and without ($E_{\rm slab}$) n metal adsorbates, and referred to energies of isolated metal atoms ($E_{\rm M}$). Since adatom charges obtained with the alternative exchange-correlation functionals are sensibly similar, bottom panel reports LDA results only.

(3O) termination. Adsorption of metal has been shown to efficiently compensate the polarity of the oxygen-rich (3O) surface.[16–18,28] The instability of the bare polar (3O) termination makes the adsorption energies particularly large, Fig. 2(a), and provokes large electron transfers from the adatoms towards the alumina surface, which results in an ionization of the metal adsorbates, Fig. 2(b). The adsorption energies are by far the largest for the elements at the beginning of the considered series (Cr, Co) and become progressively smaller when moving towards its end (Cu, Ag). Very clearly the binding strength of Zn does not follow the monotonic decrease; it is larger than this of Ag and similar to that of Cu.[28] We note that the density of adsorbed metal adatoms impacts their oxidation state, as exemplified in Fig. 2 by results for optimal series (configurations with the lowest surface energy) and those obtained with a single adatom per (1×1) cell. While adsorption energies do depend on the adatom density, we stress that the overall well pronounced decrease of $E_{\rm ads}$ along the transition series is not altered by the choice of a particular surface configuration.

The trend in adsorption energetics is also fairly insensitive to the level of approximation used for the exchange-correlation functional. Indeed, both standard LDA and GGA functionals produce the same behavior of $E_{\rm ads}$ with, as expected, systematically larger LDA adsorption energies. However, since the ionization of the adsorbed transition metal M adatoms may be seen as a formation of mixed surface oxides involving transition metal ions, the validity of the standard LDA/GGA description of the electronic structure may be questioned. We find that the results obtained within GGA+U approximation with $U-J = 4$ eV and 6 eV, typical for the corresponding transition metal oxides, produce systematically the same trend along the series, Fig. 2(a).

The decrease of adatom binding strength along the series is to be assigned principally to the progressive increase of the element electronegativity and of its metallic radius.[17] Here, we stress that, since the adsorption at this alumina termination can be seen as a formation of a surface oxide, a semi-quantitative estimate of the binding strength can be obtained directly from the measured formation enthalpies of the corresponding M_xO_y oxides [$\Delta_f H^\circ_{M_xO_y}(298.15K)$] and of isolated metal

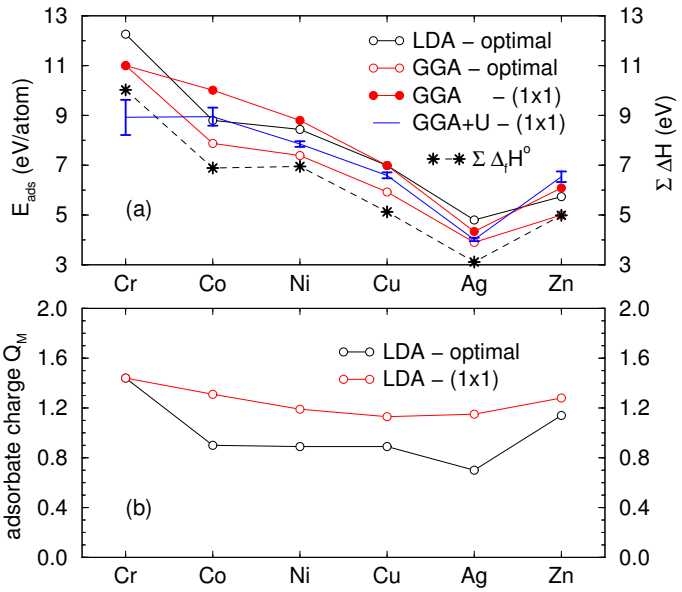

Fig. 2 (a): Adsorption energies of transition metal adatoms on a bare (3O) termination of Al_2O_3(0001) obtained at different levels of approximation. $U-J = 4$ eV and 6 eV were used in GGA+U calculations - the corresponding results are represented with the upper and lower limits of the vertical error-bars. Experimental values of oxide formation energies $\Sigma\Delta H$ are plotted to identify trends along the series - see text for details. (b): Charges of the metal adatoms deduced from LDA charge densities.

M atoms [$\Delta_f H^\circ_{M_{gas}}(298.15K)$]:[45,46]

$$E_{\rm ads} \sim \Sigma\Delta H = -\Delta_f H^\circ_{M_xO_y}/x + \Delta_f H^\circ_{M_{gas}}.$$

We note that, despite the very different structure of the native bulk and the present surface oxides, the calculated adsorption energies of the "optimal" series correlate systematically well with $\Sigma\Delta H$ of the oxide phase (Cr_2O_3, CoO, NiO, CuO, AgO, and ZnO) with the same oxidation state of the cations, Fig. 2(a).

Finally, in the context of the present study on metal-alumina interaction strength, it is worth comparing the calculated metal adsorption $E_{\rm ads}$ and metal cohesion $E_{\rm coh}$ energies. Since in all cases $E_{\rm ads} > E_{\rm coh}$, the calculated metal-oxide bonding is systematically stronger than the metal-metal one. This suggests a good wetting of the (3O) termination by all the considered metals.

(Al) termination. In the case of adsorption on the (Al) termination, Fig. 3, although the interaction strength along the series follows a trend similar to that at the (3O) surface, the $E_{\rm ads}$ is systematically much smaller,[19–21,28,47] and so is the adsorbate-substrate charge transfer at the (Al) termination. The slight decrease of $E_{\rm ads}$ in the case of Cr adsorption is to be assigned to the particular stability of the isolated Cr atom, characterized by a large magnetic moment, which is substantially quenched by the interaction with the alumina surface.

At the (Al) termination, the trend in adsorption characteristic is little influenced by the level of approximation. The adsorption energies being systematically smaller compared to the (3O) surface, the difference between LDA and GGA results becomes more apparent, but is still of the same order as at the (3O) termination.

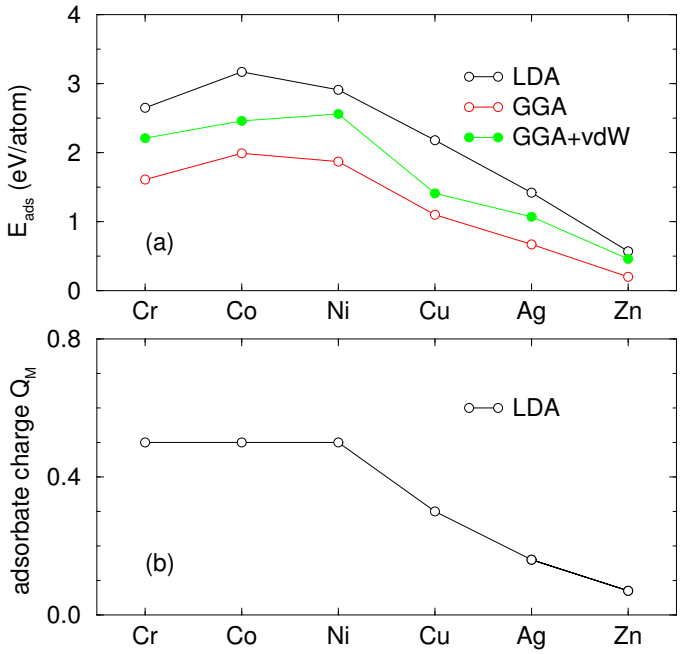

Fig. 3 (a): Adsorption energies of transition metal adatoms on the bare (1x1)-(Al) termination of Al_2O_3(0001) obtained at different levels of approximation. (b): Charges of the metal adatoms deduced from LDA charge densities.

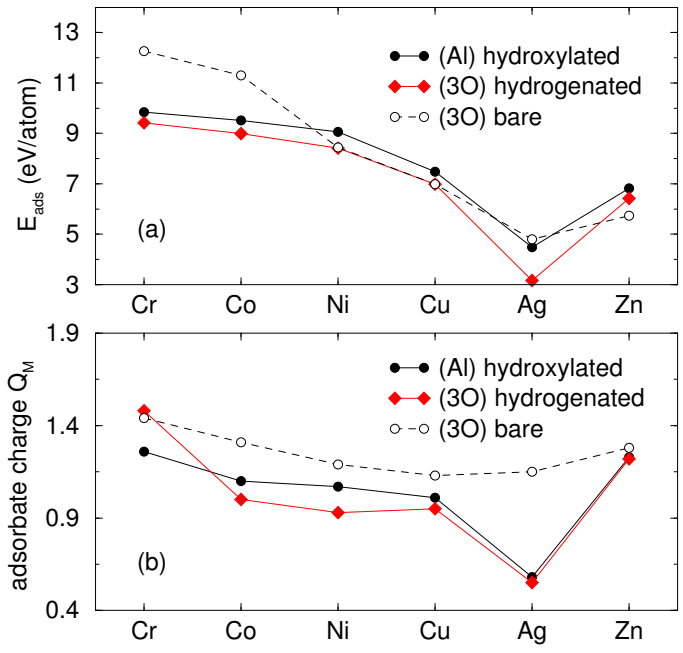

Fig. 4 LDA adsorption energies E_{ads} (eV/atom) (a) and charges Q_M (b) of isolated metal adatoms on the hydroxylated (Al) and (3O) terminations. Corresponding (LDA) data obtained for the dry (3O) termination, Fig. 2(a), are re-plotted as a reference.

More interestingly, since the adsorption energies become particularly small for the elements at the end of the series, the role of the van der Waals interactions, absent in standard LDA/GGA approximations, may become non-negligible.[48] As exemplified with the results obtained with the dispersion-corrected optB88-vdW functional, the account for the van der Waals contribution does indeed enhance the GGA interaction strength, and makes the calculated E_{ads} approach those obtained in LDA.

The behavior of the metal binding strength at the (Al) termination is fully consistent with the trends reported in the literature.[49] It is driven principally by the position of the adatom frontier orbitals with respect to the alumina band structure, and can be linked to the behavior of metal electronegativity along the series. Adsorption weakening due to the progressive increase of electronegativity in the series is additionally reinforced by the progressive increase of atomic radius of the adatoms. Both effects are also responsible for the observed decrease of the charge transfer. Joint effect of large size and large electronegativity results in a particularly weak bonding of late transition and noble metal adatoms. We note that the particularly weak adsorption of Zn is not directly expected from its moderate electronegativity, but is to be assigned to the closed shell $d^{10}s^2$ valence configuration of the isolated adatoms.[28]

Contrary to the case of the (3O) termination, a poor wetting of the (Al) surface by all considered elements can be expected from the adsorption energies, which are much smaller than the metal cohesion energies ($E_{ads}/E_{coh} < 0.5$).

Hydroxylated (Al) and (3O) surfaces. Full surface hydrogenation [(3O)3H per (1×1) cell] does efficiently compensate the polarity of the oxygen-rich (3O) termination and makes it thermodynamically favored in hydrogen-rich environments.[50–55] We have recently shown that polarity compensation can also be achieved by a joint effect of co-adsorbed zinc and hydrogen, such that the charge neutral surface configuration, with a single Zn adatom replacing two out of the three surface hydrogens in the (1×1) cell [(3O)HZn], is thermodynamically favored at intermediate hydrogen conditions.[28] Similar metal ↔ hydrogen exchange has been shown to efficiently stabilize the otherwise weakly bound late transition metal adatoms (Co, Cu, Ag) at the hydroxylated neutral [(Al)OHH per (1×1) cell] alumina termination.[22–24,56] This mechanism is operational also in the case of Zn adsorption, with the optimal stability for the charge neutral surface configuration (Al)$OHZn_{0.5}$.[28]

Figure 4 summarizes the calculated adsorption characteristics of metal M adatoms obtained for the optimal surface configurations on the hydroxylated (Al) and hydrogenated (3O) terminations. We focus here only on the strongly bound configurations, produced upon exchange of metal adatom with surface hydrogens. Since, as discussed before, the results obtained at different levels of approximation follow the same trends, we limit the presentation to the LDA results only.

We find that the metal binding strength on both hydroxylated terminations is systematically large, close to that on the bare (3O) surface, Fig. 4(a). Adsorption is accompanied by a similarly strong electron transfer towards the hydroxylated oxide substrate, consistent with ionization of the adsorbed metal species, Fig. 4(b). These results show that the binding mechanism described previously for the late transition and noble metals[22–24,28,56] applies systematically also to other elements of the transition series. Moreover, the behavior of E_{ads} along the series

follows very closely that obtained for the bare (3O) surface. The elements from the beginning of the considered series (Cr, Co) bind more strongly to the hydroxylated alumina surfaces, and the adsorption strength weakens progressively towards the end of the series. These similarities suggest that, alike at the bare (3O) surface, it is the energetics of surface hydroxide formation which drives the behavior of the interaction strength along the series. However, while matching of $E_{\rm ads}$ on the three terminations is very good for most of the considered metals, the adsorption of Cr and Co in presence of surface hydroxyls is visibly weaker than that at the bare (3O) surface. Since metal adsorption on hydroxylated terminations results in formation of mixed (Al,M)$(OH)_x$ hydroxide surface species, the above difference with respect to adsorption at the bare (3O) termination is consistent with the low stability of Cr and Co hydroxides.

4 Thermodynamic stability of weakly and strongly bound adatoms.

The adsorption energies of metal adatoms at α-alumina (0001) surfaces of different polar characters and different degrees of surface hydroxylation discussed above enable the construction of a thermodynamic stability diagram of alternative surface configurations.[28,57] For each given oxygen/hydrogen environment [defined by the corresponding oxygen and hydrogen chemical potentials $\Delta\mu_{\rm O}$ and $\Delta\mu_{\rm H}$, which can be linked to the temperature T and to partial pressures p_i (i = O, H) of the gas atmosphere $\Delta\mu_i$(T, p_i) = $\Delta\mu_i$(T, p_0) + $\frac{1}{2}kTln(p_i/p_0)$], such diagram displays the surface configuration with the lowest grand potential:

$$\gamma(\Delta\mu_{\rm O},\Delta\mu_{\rm H}) = \gamma^{\rm bare}(\Delta\mu_{\rm O},\Delta\mu_{\rm H}) - n(E_{\rm ads}-E_{\rm coh})/S$$

In the above expression, γ and $\gamma^{\rm bare}$ represent energies of alumina surface with and without metal adsorbates, respectively. $E_{\rm ads}$ and $E_{\rm coh}$ are metal adsorption and metal cohesion energies, and n/S is the surface density of adsorbed metal adatoms. The chosen metal bulk $E_{\rm coh}$ reference is particularly well suited for the identification of configurations with strongly bound metal adatoms ($E_{\rm ads} > E_{\rm coh}$). Moreover, it also enables a partial cancellation of the spurious over- and under-binding trends typical for LDA and GGA, respectively. As exemplified by the case of Zn adsorbate, both LDA and GGA give a qualitatively similar picture of relative surface stability. The differences concern principally the stability limits of surface configurations on the $\Delta\mu_{\rm O}$ scale (LDA systematically shifts the transition lines towards more oxygen-lean conditions).

Thermodynamic stability diagrams for α-alumina(0001) surfaces with Cr, Ni, Ag, or Zn adatoms are displayed in Fig. 5. $\Delta\mu_{\rm O/H} \sim$ 0.0 eV correspond to oxygen/hydrogen-rich conditions (condensation of oxygen/hydrogen molecules). Conversely, $\Delta\mu_{\rm O} \sim$ -6.0 eV and $\Delta\mu_{\rm H} \sim$ -4.0 eV represent extreme oxygen/hydrogen-poor conditions. In particular, the latter represents oxygen conditions at which bulk alumina decomposes. In the following we focus principally on the conditions of thermodynamic stability of surface configurations with strongly bound metal M adatoms discussed in Section 3. These include M adatoms on bare (3O) termination [(3O)M_y] as well as on

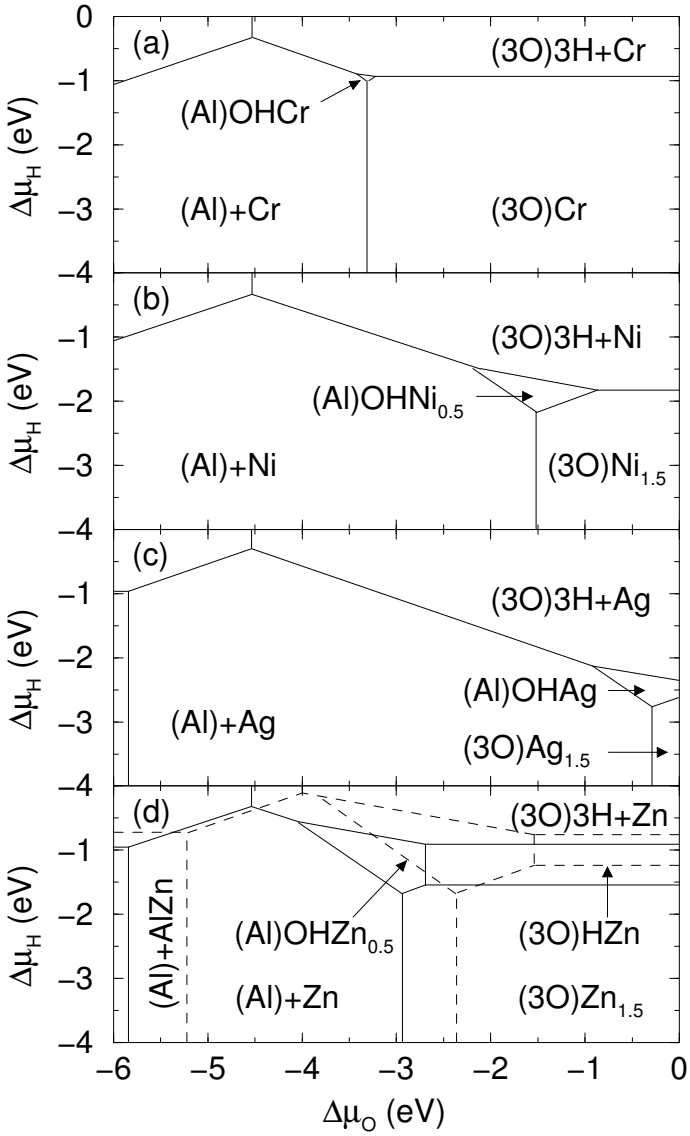

Fig. 5 Thermodynamic stability diagrams (LDA) of the most stable configurations of Al_2O_3(0001) surface with (a) Cr, (b) Ni, (c) Ag, and (d) Zn adatoms as a function of oxygen and hydrogen chemical potentials $\Delta\mu_{\rm O}$ and $\Delta\mu_{\rm H}$. In case of Zn, the corresponding GGA results are plotted with dashed lines. Compositions of surface configurations [per (1×1) cell] are explicitly indicated.

hydroxylated (Al) and (3O) terminations [(Al)$(OH)_xM_y$ and (3O)H_xM_y, respectively]. In all cases, stability conditions of bare (Al) and fully hydrogenated (3O)3H terminations with weakly adsorbed metal [(Al)+M and (3O)3H+M, respectively] are displayed as a reference. Corresponding structural data is provided in supplementary information.†

The diagrams in Fig. 5 show that in all cases an adequate change of thermodynamic conditions ($\Delta\mu_O$, $\Delta\mu_H$) may indeed produce a qualitative change in the nature of thermodynamically favored adatom binding from weak and non-wetting to strong and perfectly wetting. In the absence of surface hydrogen ($\Delta\mu_H \sim$ -3 eV) the critical condition is defined solely by the oxygen chemical potential $\Delta\mu_O^c$, which delimits the stability ranges of weakly bound (Al)+M and strongly bound (3O)M_y surface configurations. In the considered series $\Delta\mu_O^c$ varies progressively from oxygen-poor conditions in case of Cr and Zn ($\Delta\mu_O^c \sim$ -3.3 eV and -2.9 eV, respectively), through oxygen-moderate conditions for Ni ($\Delta\mu_O^c \sim$ -1.5 eV), up to oxygen-rich conditions in the case of Ag ($\Delta\mu_O^c \sim$ -0.3 eV). The behavior of $\Delta\mu_O^c$ along the series is driven principally by the relative stability of adatoms strongly bound to the bare (3O) surface and those integrated into metallic clusters, weakly bound to the (Al) termination. It can be quantified by the difference between the metal adsorption energy on the (3O) surface $E_{ads}^{(3O)}$ and the metal cohesion energy E_{coh}: $\Delta\mu_O^c \sim E_{ads}^{(3O)} - E_{coh}$. Since, as argued in Section 3, the behavior of $E_{ads}^{(3O)}$ is directly linked to $\Sigma\Delta H$ and E_{coh} can be estimated with $\Delta_f H^\circ_{M_{gas}}(298.15K)$, the behavior of $\Delta\mu_O^c$ follows that of the oxide formation energy: $\Delta\mu_O^c \sim \Delta_f H^\circ_{M_xO_y}(298.15K)/x$. Indeed, large $\Delta_f H^\circ$ in the case of Cr results in large $\Delta\mu_O^c$, while the particularly small $\Delta_f H^\circ$ of Ag produces $\Delta\mu_O^c$ close to zero. We note that a relatively large $\Delta\mu_O^c$ in the case of Zn is principally due to the small cohesion energy of zinc.

In the presence of surface hydroxyls, the strongly bound configuration (Al)$(OH)_xM_y$ may be stabilized. In the considered series of adatoms, this configuration hardly appears in the Cr diagram [Fig. 5(a)], but is clearly present in those of Ni, Ag and Zn [Figs. 5(b)-(d)], as well as in this of Cu reported in Ref.[28]. The presence of the (Al)$(OH)_xM_y$ configuration in the stability diagram is to be linked to the difference of adsorption energies $E_{ads}^{(Al)hyd}$ - $E_{ads}^{(3O)}$ at hydroxylated (Al) and bare (3O) surfaces, respectively. Indeed, in agreement with the data reported in Fig. 4(a), these configurations become thermodynamically stable only for elements for which difference of $E_{ads}^{(Al)hyd}$ and $E_{ads}^{(3O)}$ is small: Ni, Cu, Ag, and Zn. If present, the (Al)$(OH)_xM_y$ is stabilized in oxygen conditions close to $\Delta\mu_O^c$. Moreover, since its stability region lies at the transition line between the dry (Al) and the hydroxylated (3O) surfaces, its critical hydrogen condition $\Delta\mu_H^c$ varies in the direction opposite to that of oxygen: $\Delta\mu_H^c \sim -\Delta\mu_O^c$. As a consequence $\Delta\mu_H^c$ corresponds to hydrogen-rich and moderate conditions for Cr ($\Delta\mu_H^c \sim$ -1.0 eV), Zn ($\Delta\mu_H^c \sim$ -1.3 eV) and Ni ($\Delta\mu_H^c \sim$ -1.8 eV), but to particularly hydrogen-poor conditions for Ag ($\Delta\mu_H^c \sim$ -2.5 eV).

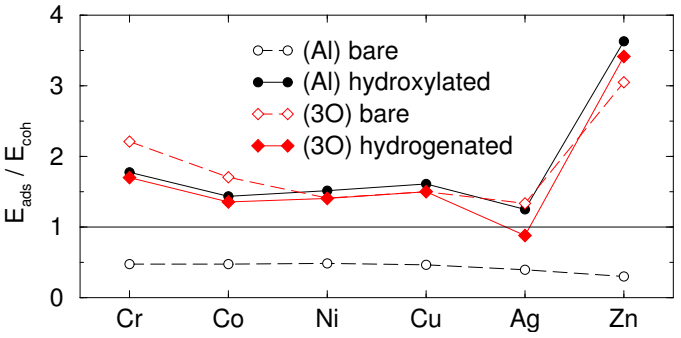

Fig. 6 Ratio of calculated adatom adsorption and metal cohesion energies (LDA) for the four types of considered alumina terminations. Adsorption energies correspond to the optimal surface configurations for each of the terminations.

5 Discussion of Zn/alumina interface resistance

As a first element of the discussion on adhesion at metal/alumina interface, Fig. 6 reports the ratio of adatom adsorption and metal cohesion energies at the four types of considered alumina surfaces, which can be used for a rough estimation of surface wetting by the corresponding metal deposit. Very clearly, with respect to Zn adatoms interacting weakly with the non-polar (Al) termination, a substantial enhancement of the interaction strength can be gained by the use of either the polar bare or hydrogenated (3O) surface or the hydroxylated non-polar (Al) termination. We note that, compared to other metals, the associated improvement of wetting is expected to be particularly large for Zn, due principally to its relatively low cohesion energy. Moreover, these results suggest that an addition of transition metals such as Cr or Co may substantially improve the metal-oxide interaction with the bare (Al) termination. The above estimation gives valid grounds for a more quantitative approach to possible ways to improve the adhesion of the Zn/alumina interface. Beyond the results on adatom adsorption reported in preceding section, in the following we will argue that interface adhesion is indeed improved by these mechanisms.

Figure 7 represents schematically the three model interfaces considered herein: zinc surface in direct contact with either the bare (Al) or bare (3O) alumina terminations, and zinc separated from the (Al) surface by a Cr buffer. At the (Al)/Zn interface Zn atoms occupy preferentially O-top sites, whereas at the (3O)/Zn they are located on-top of Al ions. In the (Al)/Cr/Zn system, Cr atoms favor Al-top sites of alumina at the (Al)/Cr interface, and are located in hollow sites of the Zn surface at the Cr/Zn interface. Corresponding structural data is provided in supplementary information.†The results reported in Tab. 1 refer to a Cr three-layer, but similar effect was also obtained with one- and two-layer-thick Cr buffers. The adhesion strengths at different points of the three superstructures (indicated by arrows in Fig. 7) are estimated from separation energies $E_{sep} = (-E_{A/B} + E_A + E_B)/(2S)$, where $E_{A/B}$, E_A, and E_B are the total energies of respectively the A/B superstructure and separate A and B slabs. Factor 2 accounts for the two equivalent A/B interfaces in each periodic unit cell used in

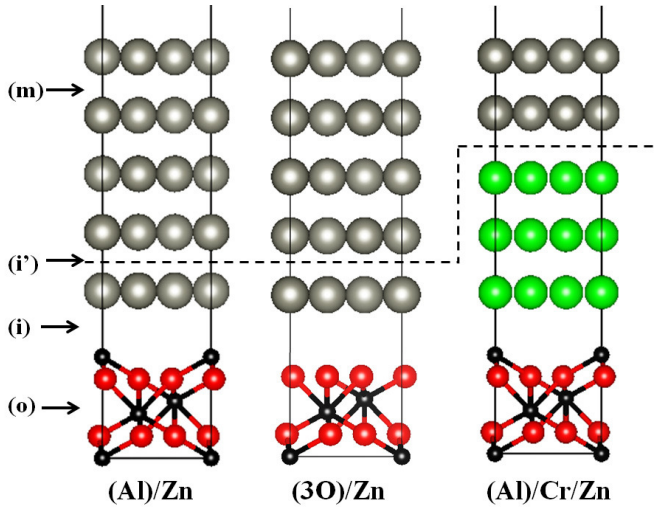

Fig. 7 Schematic representation of alumina/Zn interfaces with either (Al) or (3O) termination in contact with the zinc. In case of the (Al)/Zn interface an additional Cr buffer is considered. Arrows indicate the considered separation zones: in the oxide (o), at the interface (i)-(i'), and in the metal (m). Oxygen, aluminum, zinc and chromium atoms are represented with red, black, grey, and green circles, respectively.

calculations and S is the interface area. Table 1 reports the separation energies calculated for the bulk Al_2O_3 (o) and bulk Zn (m), as well as these obtained for the Al_2O_3/metal (i) and metal/metal (i') interfaces.

The three types of exchange-correlation functionals used in the study produce the same pattern in behavior of the adhesion strength. As expected from the results on the adsorption of isolated Zn atoms, we find only a very weak adhesion for the (Al)/Zn system, with the separation energy at the alumina/zinc interface smaller than that in the zinc and alumina crystals. This clearly identifies the least resistant region to be the very metal/oxide interface, and predicts an interfacial cleavage.

The situation is qualitatively different in the (3O)/Zn system, for which the separation energy at the very interface is larger than both in the bulk oxide and in the bulk Zn. Interestingly, in this case the enhanced adhesion strength at the interface and the associated ionization of Zn in contact with the oxide do not impact considerably the Zn-Zn interaction in the direct vicinity of the interface. Very clearly, the overall interface resistance is limited only by that of the bulk Zn, pointing to a cohesive cleavage.

Most interestingly, as exemplified by the (Al)/Cr/Zn system, a Cr buffer at the (Al)/Zn interface strengthens the adhesion. While adhesion at the (Al)/Cr interface is smaller compared to the polar (3O)/Zn, it remains considerably larger than that in the bulk Zn. Since the adhesion at the Cr/Zn interface is large, the overall interface resistance is limited by that of the bulk Zn, which again favors a cohesive cleavage.

While these findings will be extended in a forthcoming study, as to take into account the possibility of interface inter-diffusion, metal alloying, and oxidation, at the present stage we can predict that an enrichment of the non-polar (Al)/Zn interface with a transition metal, as represented by the model case of a Cr buffer, strengthens the interface to the point that it becomes cohesive.

Table 1 Separation energies (J/m^2) at different fracture zones of the three considered systems, as obtained from LDA, GGA, and GGA+vdW calculations. Location of the most weakly adhering atomic layers is indicated in bold.

	(o)	(i)	(i')	(m)
LDA				
(Al)/Zn	4.16	**0.72**	1.28	1.54
(3O)/Zn	4.16	7.90	1.84	**1.54**
(Al)/Cr/Zn	4.16	2.59	3.89	**1.54**
GGA				
(Al)/Zn	3.27	**0.34**	0.78	0.79
(3O)/Zn	3.27	6.54	0.91	**0.79**
(Al)/Cr/Zn	3.27	1.82	2.94	**0.79**
GGA+vdW				
(Al)/Zn	3.88	**0.78**	1.04	1.08
(3O)/Zn	3.88	7.31	1.12	**1.08**
(Al)/Cr/Zn	3.88	2.12	3.33	**1.08**

A similar, or even stronger resistance is expected at the polar (3O)/Zn interface, which, however, may be less straightforward to use in practice, due to instability of the bare (3O) alumina termination. In this case, alternative routes involving mixed interface (Al,Zn) oxides or hydroxides are to be explored.

6 Conclusions

We have used *ab initio* total energy calculation to study the interaction between transition metal adatoms and various bare and hydroxylated α-alumina(0001) surfaces. In a comprehensive manner, by focusing only on the most representative surface configurations, we have evidenced a clear trend in the adsorption characteristics and in the relative stability of surface configurations involving weakly and strongly bound ad-atoms, which is little dependent on the polar/non-polar character of the surface termination and on its precise hydroxylation state. In particular, due to its small electronegativity and small size, chromium has been identified as particularly well interacting, regardless the precise thermodynamic conditions.

Guided by the results on the adatom adsorption, we have performed a preliminary analysis of adhesion strength at several prototypical constituted Zn/alumina interfaces. We have shown that, with respect to the weakly adhesive case of Zn in contact with bare stoichiometric alumina termination, a substantial gain of interface resistance can be achieved by either the use of oxygen-rich polar alumina termination, or, more interestingly, by interface enrichment in transition metal such as Cr. While, due to instability of the oxygen-rich alumina termination, the former may be less straightforward to implement in practical realizations, the latter points to a very promising route for industrial applications.

7 Acknowledgments

The authors are grateful to Claudine Noguera and Jean-Michel Mataigne for many fruitful discussions, they acknowledge (R.C. and H.-L.T.L.) the financial support from ArcelorMittal Maizières Research, and a generous allocation of computing time at IDRIS, under Project No. 100170.

References

1 K. L. Choy, *Prog. Mater. Sci.*, 2003, **48**, 57–170.

2 J. E. Gray and B. Luan, *J. Alloys Compd.*, 2002, **336**, 88–113.

3 D. E. Tallman, G. Spinks, A. Dominis and G. G. Wallace, *J. Solid State Electrochem.*, 2002, **6**, 73–84.

4 D. Wang and G. R. Bierwagen, *Prog. Org. Coat.*, 2009, **64**, 327–338.

5 W. Lee and S.-J. Park, *Chem. Rev.*, 2014, **114**, 7487–7556.

6 A. R. Marder, *Prog. Mater. Sci.*, 2000, **45**, 191–271.

7 M. Guttmann, *Materials Science Forum*, 1994, **155-156**, 527–548.

8 G. Beranger, G. Henry and G. S. (Eds.), *The Book of Steel*, Lavoisier Publishing, Intercept LTD, 1996, pp. 1268–1278.

9 M.-L. Giorgi, J. Diawara, S. Chen, A. Koltsov and J.-M. Mataigne, *J. Mater. Sci.*, 2012, **47**, 8483–8495.

10 P. Drillet, Z. Zermout, D. Bouleau, J.-M. Mataigne and S. Claessens, *Rev. Metall.-Cah. Inf. Tech.*, 2004, **10**, 831–837.

11 O. Grässel, L. Krüger, G. Frommeyer and L. W. Meyer, *International Journal of Plasticity*, 2000, **16**, 1391–1409.

12 H.-T. Jiang, W. Ding, D. Tang and W. Huang, *J. Iron and Steel Research*, 2012, **19**, 29–36.

13 I. Nikulin, T. Sawaguchi and K. Tsuzaki, *Materials Science and Engineering A*, 2013, **587**, 192–200.

14 W. Wang, M. Li, C. He, X. Wei, D. Wang and H. Dub, *Materials and Design*, 2013, **47**, 510–521.

15 A. Mertens, E. M. Bellhouse and J. R. McDermid, *Materials Science & Engineering A*, 2014, **608**, 249–257.

16 C. Verdozzi, D. R. Jennison, P. A. Schultz and M. P. Sears, *Phys. Rev. Lett.*, 1999, **82**, 799–802.

17 A. Bogicevic and D. R. Jennison, *Phys. Rev. Lett.*, 1999, **82**, 4050–4053.

18 I. G. Batyrev, A. Alavi and M. W. Finnis, *Phys. Rev. B*, 2000, **62**, 4698–4706.

19 D. J. Siegel, J. L. G. Hector and J. B. Adams, *Phys. Rev. B*, 2002, **65**, 085415.

20 N. C. Hernandez, J. Graciani, A. Márquez and J. F. Sanz, *Surf. Sci.*, 2005, **575**, 189–196.

21 L. G. V. Briquet, C. R. A. Catlow and S. A. French, *J. Phys. Chem.*, 2008, **112**, 18948–18954.

22 C. Niu, K. Shepherd, D. Martini, J. Tong, J. A. Kelber, D. R. Jennison and A. Bogicevic, *Surf. Sci.*, 2000, **465**, 163–176.

23 J. A. Kelber, C. Niu, K. Shepherd, D. R. Jennison and A. Bogicevic, *Surf. Sci.*, 2000, **446**, 76–88.

24 S. A. Chambers, T. Droubay, D. R. Jennison and T. R. Mattsson, *Science*, 2002, **297**, 827–831.

25 R. Triboulet and J. Perriere, *Progress in Crystal Growth and Characterization of Materials*, 2003, **47**, 65–138.

26 J. A. Rodriguez, M. Kuhn and J. Hrbek, *J. Phys. Chem.*, 1996, **100**, 18240–18248.

27 R. Lazzari, J. Jupille, R. Cavallotti and I. Simonsen, *J. Phys. Chem. C*, 2014, **118**, 7032–7048.

28 R. Cavallotti, J. Goniakowski, R. Lazzari, J. Jupille, A. Koltsov and D. Loison, *J. Phys. Chem. C*, 2014, **118**, 13578–13589.

29 R. Cavallotti, *Ph.D. thesis*, Université Pierre et Marie Curie (UPMC), Paris, France, 2014.

30 G. Kresse and J. Furthmuller, *Phys. Rev. B*, 1996, **54**, 11169–11186.

31 G. Kresse and J. Hafner, *Phys. Rev. B*, 1993, **47**, 558–561.

32 P. E. Blöchl, *Phys. Rev. B*, 1994, **50**, 17953–17979.

33 G. Kresse and J. Joubert, *Phys. Rev. B*, 1999, **59**, 1758–1775.

34 J. P. Perdew and A. Zunger, *Phys. Rev. B*, 1981, **23**, 5048–5079.

35 J. P. Perdew, J. A. Chevary, S. H. Vosko, K. A. Jackson, M. R. Pederson, D. J. Singh and C. Fiolhais, *Phys. Rev. B*, 1992, **46**, 6671–6687.

36 M. Dion, H. Rydberg, E. Schroder, D. C. Langreth and B. I. Lundqvist, *Phys. Rev. Lett.*, 2004, **92**, 246401.

37 J. Klimes, D. R. Bowler and A. Michaelides, *J. Phys.: Cond. Matt.*, 2010, **22**, 022201.

38 J. Klimes, D. R. Bowler and A. Michaelides, *Phys. Rev. B*, 2011, **83**, 195131.

39 S. L. Dudarev, G. A. Botton, S. Y. Savrasov, C. J. Humphreys and A. P. Sutton, *Phys. Rev. B*, 1998, **57**, 1505–1509.

40 C. Noguera, *J. Phys.: Condens. Matter*, 2000, **12**, R367–R410.

41 J. Goniakowski, F. Finocchi and C. Noguera, *Rep. Prog. Phys.*, 2008, **71**, 016501–016555.

42 R. F. W. Bader, *Chem. Rev.*, 1991, **91**, 893–928.

43 G. Henkelman, A. Arnaldsson and H. Jonsson, *Comput. Mater. Sci.*, 2006, **36**, 354–360.

44 W. Tang, E. Sanville and G. Henkelman, *J. Phys.: Condens. Matter*, 2009, **21**, 084204–084207.

45 J. M. W. Chase, *J. Phys. Chem. Ref. Data*, 1998, **Monograph 9**, 1–1951.

46 J. D. Cox, D. D. Wagman and V. A. Medvedev, *CODATA Key Values for Thermodynamics*, Hemisphere Publishing Corp., New York, 1984.

47 V. V. Melnikov, S. V. Yeremeev and S. E. Kulkova, *Russ. Phys. J.*, 2011, **54**, 704–712.

48 F. Didier and J. Jupille, *Surf. Sci.*, 1994, **314**, 378–384.

49 C. T. Campbell, *Surface Science Reports*, 1997, **27**, 1–111.

50 X. G. Wang, A. Chaka and M. Scheffler, *Phys. Rev. Lett.*, 2000, **84**, 3650–3653.

51 P. J. Eng, T. P. Trainor, J. G. E. Brown, G. A. Waychunas, M. Newville, S. R. Sutton and M. L. Rivers, *Science*, 2000, **288**, 1029–1033.

52 Z. Lodziana, J. K. Norskov and P. Stoltze, *J. Chem. Phys.*, 2003, **118**, 11179–11188.

53 A. Marmier and S. C. Parker, *Phys. Rev. B*, 2004, **69**, 115409.

54 V. A. Ranea, I. Carmichael and W. F. Schneider, *J. Phys. Chem. C*, 2009, **113**, 214.

55 P. Thissen, G. Grundmeier, S. Wippermann and W. G. Schmidt, *Phys. Rev. B*, 2009, **80**, 245403.

56 R. Meyer, Q. Ge, J. Lockemeyer, R. Yeates, M. Lemanski, D. Reinalda and M. Neurock, *Surf. Sci.*, 2007, **601**, 134–145.

57 K. Reuter and M. Scheffler, *Phys. Rev. B*, 2001, **65**, 035406.